UC Davis

UC Davis Previously Published Works

Title

151Eu Mössbauer Spectroscopic and Magnetic Study of the Zintl Arsenides: Eu14MAs11 (M = Mg, Zn, Cd)

Permalink

https://escholarship.org/uc/item/2rz9s7cs

Journal

Chemistry of Materials, 38(18)

ISSN

0897-4756

Authors

Islam, MM

Shen, Z

Yumnam, G

et al.

Publication Date

2026-09-22

DOI

10.1021/acs.chemmater.6c01966

Copyright Information

This work is made available under the terms of a Creative Commons Attribution License, available at https://creativecommons.org/licenses/by/4.0/

Peer reviewed

eScholarship.org Powered by the California Digital Library
University of California

Ultra-Low Thermal Conductivity and Promising Thermoelectric Performance in the Structurally Complex Zintl Phase: $Eu_{14}GaAs_{11}$

Md. Minhajul Islam,[1] Maria Wróblewska,[2] Yixuan Xu,[1] Eric S. Toberer,[2] and Susan M. Kauzlarich[1*]

[1]Department of Chemistry, University of California, One Shields Ave, Davis, CA 95616, United States
[2]Department of Physics, Colorado School of Mines, 1500 Illinois St, Golden, CO 80401, United States

*Corresponding author: smkauzlarich@ucdavis.edu

Abstract

Intermetallic Zintl compounds of the $Ca_{14}AlSb_{11}$ (14-1-11) structure type are intriguing materials for study due to their small bandgap semiconducting behavior and exceptionally low thermal conductivity. $Eu_{14}GaAs_{11}$ is a new member of the family, containing zero-dimensional tetrahedral $[GaAs_4]^{9-}$ subunits. This compound crystallizes in the tetragonal crystal system ($I4_1/acd$ space group), similar to other 14-1-11 compounds. $Eu_{14}GaAs_{11}$ has been characterized as a semiconductor with a bandgap of 0.61 eV, as calculated using the Goldsmid-Sharp formula. Electronic transport measurements indicate a high Seebeck coefficient of 232 μV/K at 321 K, peaking at 424 μV/K at 713 K. The electrical resistivity is particularly high due to low carrier concentrations. However, the compound's notable strengths include its stability at high temperatures and its ultra-low thermal conductivity of 0.59 W m^{-1} K^{-1} at room temperature, with minimal electronic contribution, making it even lower than that of other high-performing Zintl phases. Given its low thermal conductivity and high Seebeck coefficient, $Eu_{14}GaAs_{11}$ presents potential for further optimization by adjusting the carrier concentration to enhance its thermoelectric performance.

1 Introduction

The rapid development of technology has led to the exploration of new and efficient energy generation methods. Thermoelectric materials offer an innovative solution for converting heat into electricity through the Seebeck effect.[1] By harnessing these materials, we can effectively utilize waste heat from industries, homes, and transportation, while also unlocking their potential for various other applications.[2] The performance of thermoelectric materials is characterized by the dimensionless figure of merit, zT, given by the equation, $zT = S^2T/\rho\kappa$. In this equation, S represents the Seebeck coefficient, ρ is electrical resistivity, T is the temperature, and κ is the total thermal conductivity. The total thermal conductivity is comprised of both lattice thermal conductivity and

electronic thermal conductivity. However, these properties are intrinsically interrelated as a function of carrier concentration, making it challenging to optimize one property without compromising the other. Consequently, with the advancement of machine learning (ML)-driven approaches,[3] exploring new compounds that exhibit desirable thermoelectric properties, such as low thermal conductivity or high electrical conductivity, has become a promising area of research.

Zintl phases are a subset of intermetallic compound that have emerged as prime candidates for high performing thermoelectric materials due to their unique structural characteristics, bonding properties, and the potential for optimizing carrier concentration through doping.[4] These phases exhibit salt-like behavior, with the electropositive cations donating their electrons to the more electronegative anions.[5] Furthermore, the anionic units can either be isolated or form covalent bonds and polyanionic units. Among the various structure types, $A_{14}MPn_{11}$ (14-1-11) compounds (A = Ca, Sr, Ba, Eu, Yb; M = Al, Ga, In, Mn, Zn, Cd, Mg; Pn = P, As, Sb, Bi) stand out for their high thermoelectric performance due to exceptionally low lattice thermal conductivity, with $Yb_{14}MgSb_{11}$ reaching an impressive maximum zT of 1.26.[6,7] When the metal atom, M, is trivalent (for example, Al^{3+}, Ga^{3+}, or In^{3+}), each formula unit consists of fourteen A^{2+} cations, one isolated $[MPn_4]^{9-}$ anionic tetrahedral subunit, one Pn_3^{7-} polyanionic unit, and four isolated Pn^{3-} anions. As a result, trivalent metal-containing $A_{14}MPn_{11}$ compounds are valence-balanced semiconductors. To date, only two compounds featuring the isolated anionic $[GaAs_4]^{9-}$ subunit have been reported within the 14-1-11 family, namely $Ca_{14}GaAs_{11}$ and $Sr_{14}GaAs_{11}$.[8,9] These $[GaAs_4]^{9-}$ subunit-containing compounds are expected to be small bandgap semiconductors with low carrier concentrations since group 13 elements donate three electrons to the *p*-type system, resulting in minimal electronic contribution to thermal conductivity. Additionally, the complexity of bonding, the presence of isolated structural units, the large volume, and a large number of atoms in each unit cell make these compounds ideal for exhibiting low lattice thermal conductivity.[5]

Lattice thermal conductivity is an intrinsic property of a crystal structure.[10] In solids, thermal energy is stored in both acoustic and optical phonons. In a crystalline solid containing N atoms in the unit cell, there are three acoustic phonons and $3N$ - 3 optical phonons.[11] A large number of atoms results in a significant proportion of optical phonons, which contributes minimally to thermal transport due to near-zero phonon velocity. Therefore, acoustic phonons are the primary contributor to lattice thermal conductivity because of their high phonon velocities. There are several strategies to reduce lattice thermal conductivity using hierarchical architectures.[11] However, while these methods may significantly scatter phonons, they can also detrimentally affect electrical conductivity by scattering charge carriers. In this context, compounds with inherently low lattice thermal conductivity present an intriguing starting point for thermoelectric research. The 14-1-11 compounds with 208 atoms in the unit cell, in particular, demonstrate very low lattice thermal conductivity (below 0.5 W m^{-1} K^{-1}),[12] making them particularly interesting for this purpose.

In this work, the synthesis and thermoelectric properties of the new Zintl phase, $Eu_{14}GaAs_{11}$, are reported. This discovery of $Eu_{14}GaAs_{11}$ expands the 14-1-11 family, which features a 3+ metal ion

within the tetrahedral subunit, underscoring the potential to discover more compounds of this structural type. The crystal structure was analyzed by powder X-ray diffraction (PXRD) and Rietveld refinement, yielding a good agreement between the experimental and calculated data. Additionally, the composition was investigated through scanning electron microscopy (SEM) and energy-dispersive X-ray spectroscopy (EDS), confirming the homogeneous distribution of the elements. The temperature-dependent thermal transport properties reveal remarkably low thermal conductivity, originating from an ultra-low lattice thermal conductivity. The electrical resistivity demonstrates a degenerate semiconducting behavior, while the Seebeck coefficient is relatively high, showing a bandgap of 0.61 eV. Notably, for the first time, we report the thermoelectric efficiency of a gallium-containing 14-1-11 phase, highlighting its potential for further optimization in thermoelectric applications.

2 Results and discussion

Bulk polycrystalline $Eu_{14}GaAs_{11}$ samples were synthesized using binary precursors through ball milling and high-temperature annealing. Our group has successfully adopted this method to synthesize complex ternary phases in high purity, including $Eu_{21}Zn_4As_{18}$,[13] $Yb_{14}AlSb_{11}$,[14] and $Yb_{14}ZnSb_{11}$.[12] **Fig. 1a** presents the tetragonal crystal structure of $Eu_{14}GaAs_{11}$ belonging to the $I4_1/acd$ space group. Similar to other 14-1-11 compounds, the structure contains isolated As^{3-} anions, zero-dimensional tetrahedral $[GaAs_4]^{9-}$ subunits, and Eu cations. However, in contrast to antimony and bismuth-containing 14-1-11 compounds,[15-17] the crystal structure of these containing arsenic exhibits disorder within the linear As_3^{7-} polyanionic unit.[18,19] Therefore, rather than a linear As_3^{7-} polyanionic unit, it is better represented as a combination of As_2^{4-}-dimer and an isolated As^{3-} ion. Rietveld refinement was performed on polycrystalline PXRD data of the sample, as represented in **Fig. 1b**. Lattice parameters and atomic positions were refined using GSAS-II,[20] achieving a final wR_p and reduced χ^2 value of 11.28 and 1.67, respectively. Crystallographic sites, fractions, and multiplicity derived from Rietveld refinement are provided in the Supplementary Information (SI), **Table S1**. The lattice parameters are a = 16.2983(7) Å, c = 21.7783(12) Å, and V = 5785.08(5) Å^3 for $Eu_{14}GaAs_{11}$. **Table 1** presents a comparison of the lattice parameters for all reported 14-1-11 compounds containing the $[GaAs_4]^{9-}$ tetrahedra. The lattice parameters a and c increase as cation size increases, from Ca^{2+} (1.00 Å) to Sr^{2+} (1.18 Å).[7] This trend is also observed in the rare-earth element-containing compound $Eu_{14}GaAs_{11}$, where there is a slight decrease in lattice parameters because Eu^{2+} (1.17 Å) is slightly smaller than Sr^{2+} (1.18 Å).[7]

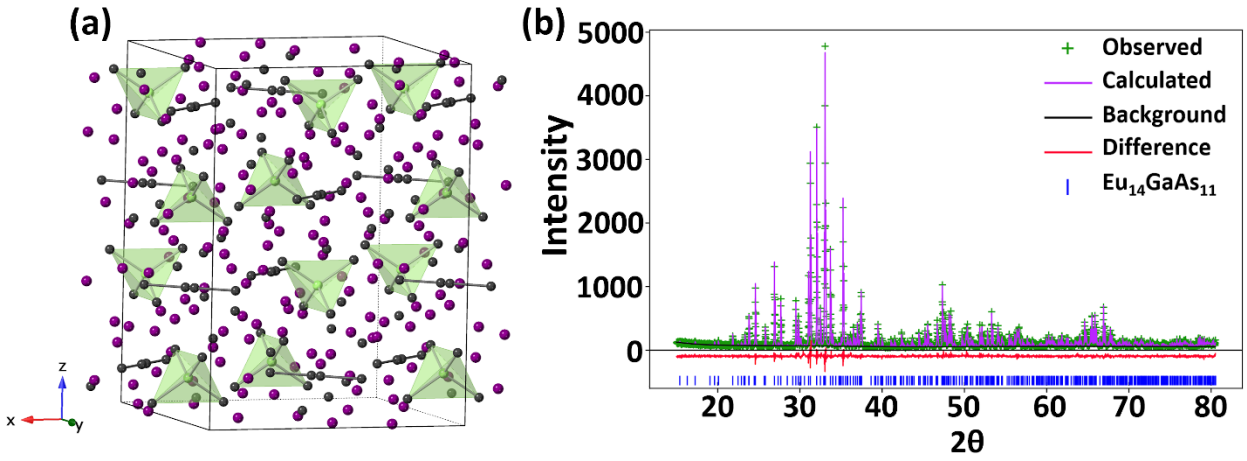


Fig. 1 (a) The crystal structure of tetragonal $Eu_{14}GaAs_{11}$, where purple spheres represent Eu, mint green spheres represent Ga, and black spheres represent arsenic. (b) Rietveld refinement of the PXRD pattern of $Eu_{14}GaAs_{11}$. The green markers correspond to observed data, the magenta line represents the calculated diffraction pattern, the red line represents the difference between observed and calculated data, and the blue lines represent the expected peaks from the crystal structure.

Table 1 Lattice parameters of $[GaAs_4]^{9-}$ subunit-containing $A_{14}GaAs_{11}$ (A = Ca, Sr, Eu) compounds

Lattice Parameter	**$Ca_{14}GaAs_{11}$[9]**	**$Sr_{14}GaAs_{11}$[8]**	**$Eu_{14}GaAs_{11}$ (This work)**
a Å	15.620(3)	16.498(8)	16.2983(7)
c Å	21.138(4)	22.132(12)	21.7783(12)
V Å^3	5157.34	6023.98	5785.08(5)

The scanning electron microscopy (SEM) images and energy-dispersive X-ray spectroscopy (EDS) elemental mapping of $Eu_{14}GaAs_{11}$ are illustrated in **Fig. 2**. The SEM images show a pore-free surface with no cracks, indicating the high density of the pressed pellet. The secondary electron (SE) image shows the pellet's surface topography and demonstrates a homogeneous distribution of the elements. The backscattered electron (BSE) image shows no variations in contrast, confirming the absence of any inclusions. Additionally, there is no aggregation or segregation of secondary phases, further confirming the sample's high purity. The EDS elemental mapping shows a well-dispersed and uniform distribution of all elements throughout the sample. There is no localized enrichment of any individual element, indicating no excess or precipitation of the reactant elements. The EDS-obtained composition is provided in the **SI**, **Table S2**.

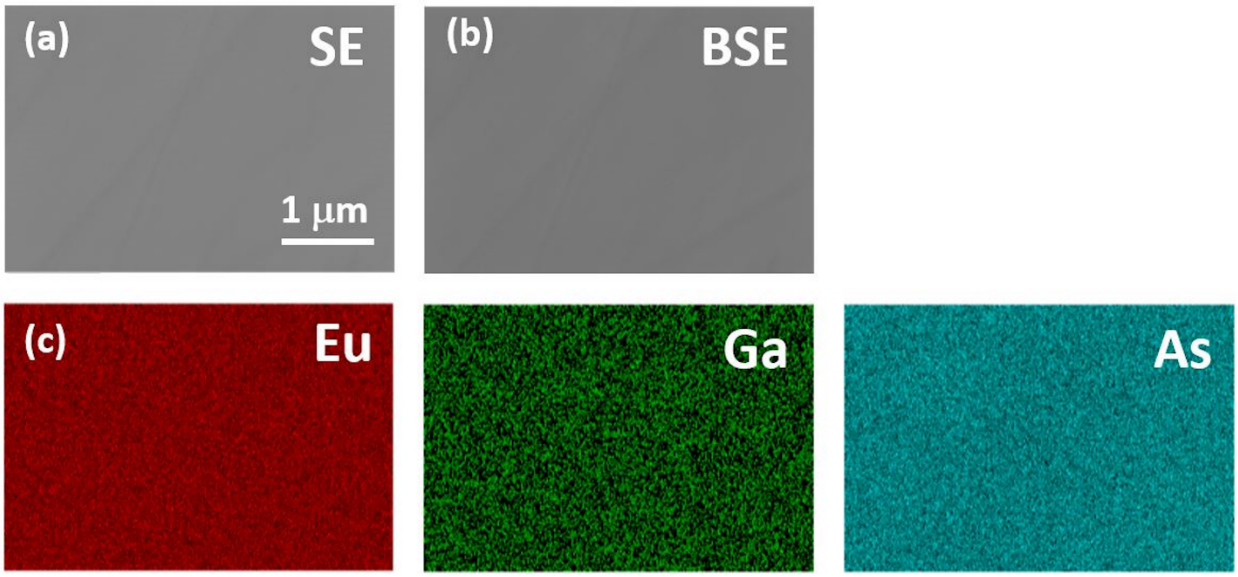


Fig. 2 (a) Secondary electron (SE) image, (b) backscattered electron (BSE) image of a pressed pellet of $Eu_{14}GaAs_{11}$, and (c) corresponding elemental mapping images of Eu, Ga, and As, respectively. The scale bar is the same for all images.

The thermal properties and stability of $Eu_{14}GaAs_{11}$ from room temperature to 1173 K have been analyzed using thermogravimetry (TG) and differential scanning calorimetry (DSC), as illustrated in **Fig. 3**. The TG curve shows no substantial mass gain, indicating that the sample did not oxidize under a flowing Ar environment. The DSC is consistent with this analysis. The upward trend in the DSC heating curve indicates that the material is undergoing sintering at high temperatures. There are no endothermic or exothermic peaks observed in the heating or cooling curves, suggesting that the phase remains stable over the measured temperature range.

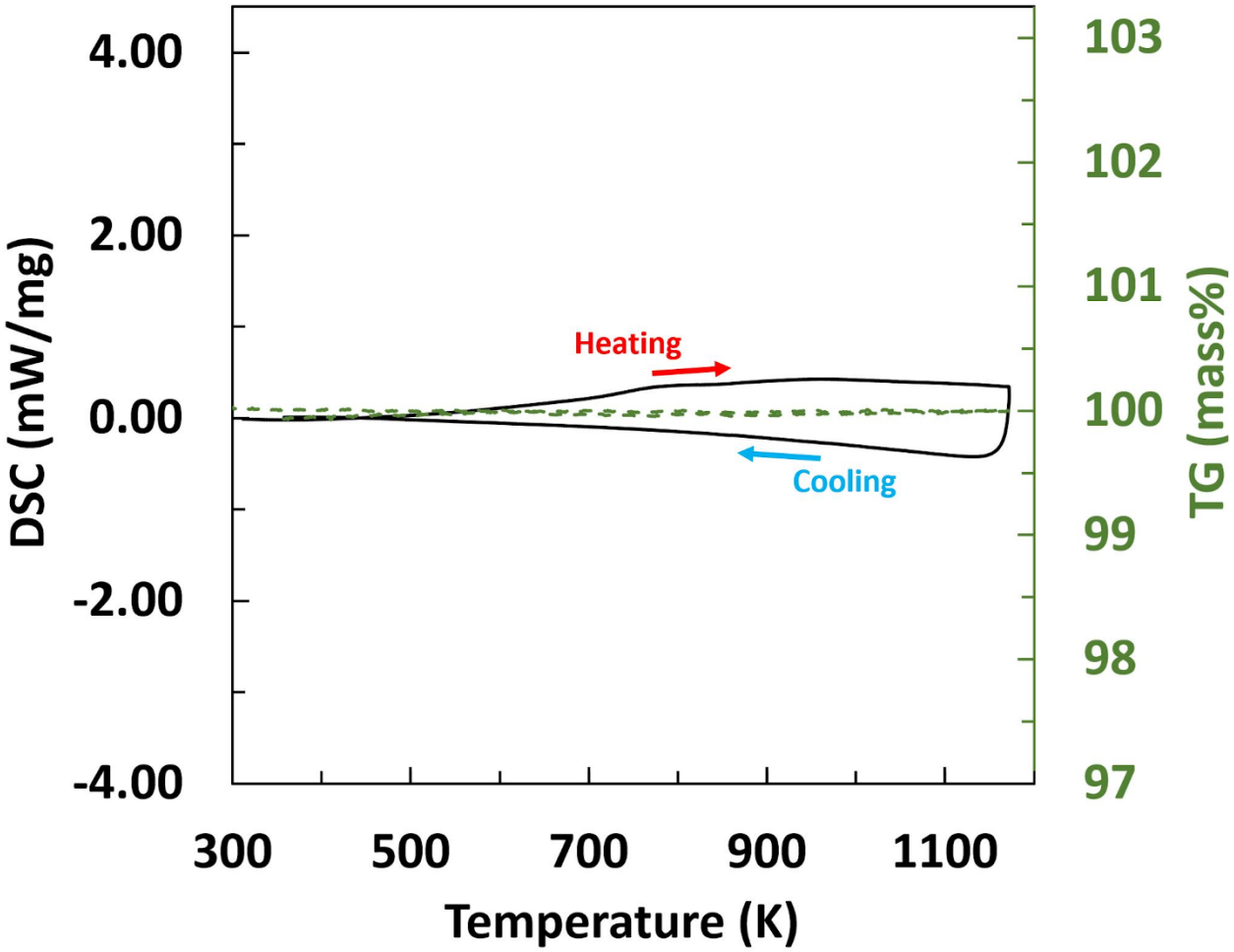


Fig. 3 Thermogravimetry (TG) and differential scanning calorimetry (DSC) of a piece of pressed pellet of $Eu_{14}GaAs_{11}$ from room temperature to 1175 K under Ar flow.

The 14-1-11 compounds show significant differences in their transport properties, despite having similar crystal structures.[7] These differences can be attributed to the varying electronegativities and bonding characteristics of the cations and pnictogen anions involved, as well as differences in total electron count. Due to the higher electronegativity of arsenic compared to antimony and bismuth, $A_{14}M\text{As}_{11}$ compounds are expected to have stronger bonding interactions, making the bonding and antibonding energy difference bigger. Consequently, arsenic-containing 14-1-11 phases typically exhibit semiconducting behavior.[7] The semiconducting nature of $Eu_{14}GaAs_{11}$ can be understood through Zintl-Klemm counting. The structure is valence-balanced, with the following charge balance: $14Eu^{2+} + [GaAs_4]^{9-} + 4As^{3-} + (As^{3-} + As_2^{4-})$.[21] As a result, the Fermi energy level for this compound, which contains a trivalent metal ion (Ga^{3+}) in the tetrahedral subunit MPn_4, is located near the valence band maximum (VBM). This is similar to the findings for Al^{3+}-containing 14-1-11 compounds by Perez *et al.* and Justl *et al.*[12,22] The electronic transport properties of $Eu_{14}GaAs_{11}$ are presented in **Fig. 4**. The electrical resistivity of $Eu_{14}GaAs_{11}$ increases with temperature, reaching a high value of 66 mΩ-cm at 336 K, as shown in **Fig. 4a**. This increase

in resistivity with temperature is commonly observed in heavily doped semiconductors and metals.[23] In **Fig. 4b**, the Seebeck coefficient of $Eu_{14}GaAs_{11}$ is presented, revealing a positive and relatively large value, which indicates *p*-type conduction in the material. The Seebeck coefficient is 232 μV/K at 321 K and reaches a peak of 424 μV/K at 713 K, indicating the onset of bipolar conduction due to minority carrier activation. Additionally, the bandgap calculated from the maximum Seebeck coefficient at that temperature, using the Goldsmid-Sharp formula ($E_g = 2eT_{max}S_{max}$), is found to be 0.61 eV.[24] The bandgaps of $Eu_{14}MAs_{11}$ (M = Mg, Zn, Cd, and Ga) compounds are listed in Table 2.

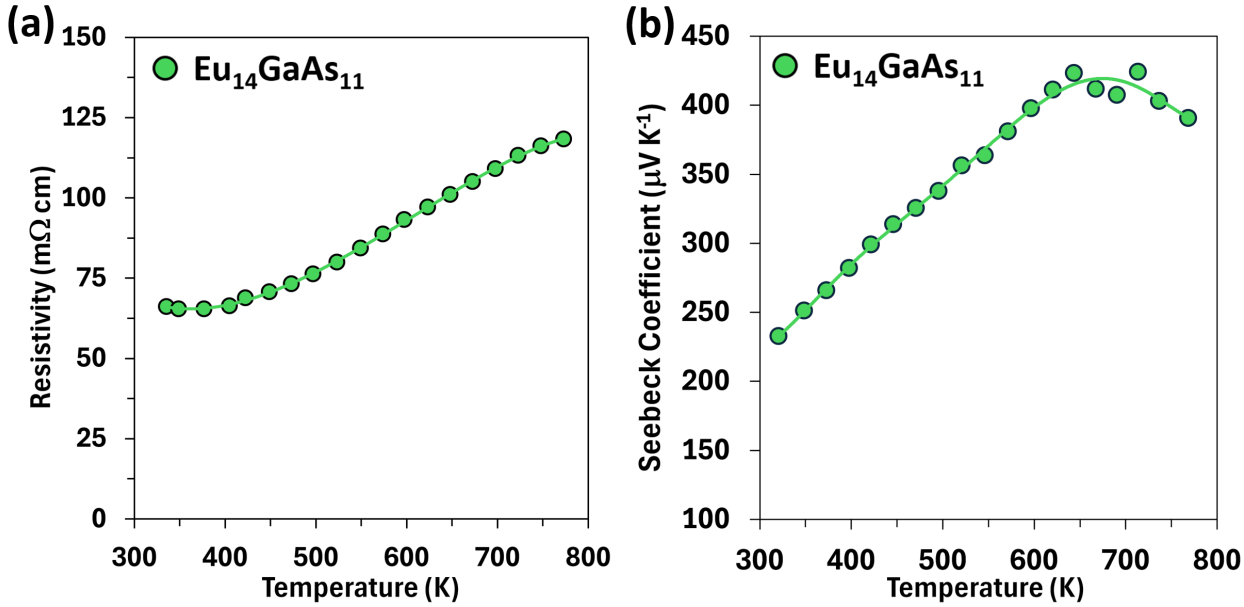


Fig. 4 Temperature-dependent (a) electrical resistivity and (b) Seebeck coefficient of $Eu_{14}GaAs_{11}$.

Table 2. Bandgap of Arsenic-containing $Eu_{14}MAs_{11}$ (M = Mg, Zn, Cd, and Ga) Compounds

Compound	Bandgap (eV)	Reference
$Eu_{14}MgAs_{11}$	0.83	[25]
$Eu_{14}ZnAs_{11}$	0.77	[25]
$Eu_{14}CdAs_{11}$	0.78	[25]
$Eu_{14}GaAs_{11}$	0.61	This work

The Hall carrier concentration and mobility of $Eu_{14}GaAs_{11}$ are illustrated in **Fig. 5**. While a trivalent metal ion (M^{3+}) subunit-containing 14-1-11 compound is typically expected to exhibit characteristics of intrinsic semiconductors with lower carrier concentrations, Ga^{3+}-containing $Eu_{14}GaAs_{11}$ demonstrates comparatively higher carrier concentrations. The Hall carrier concentration is measured at 1.24 x 10^{19} h^+ cm^{-3} at 324 K, increasing only slightly to 2.88 x 10^{19} h^+ cm^{-3} at 770 K, as illustrated in **Fig. 5a**. On the other hand, the mobility decreases with

temperature due to the scattering of charge carriers, dropping from 7.36 cm^2 V^{-1} s^{-1} at 324 K to 1.83 cm^2 V^{-1} s^{-1} at 770 K, as shown in **Fig. 5b**. At high temperatures, the mobility decreases according to a power relation of $T^{-1.5}$, indicating that mobility is primarily limited by acoustic phonon scattering.

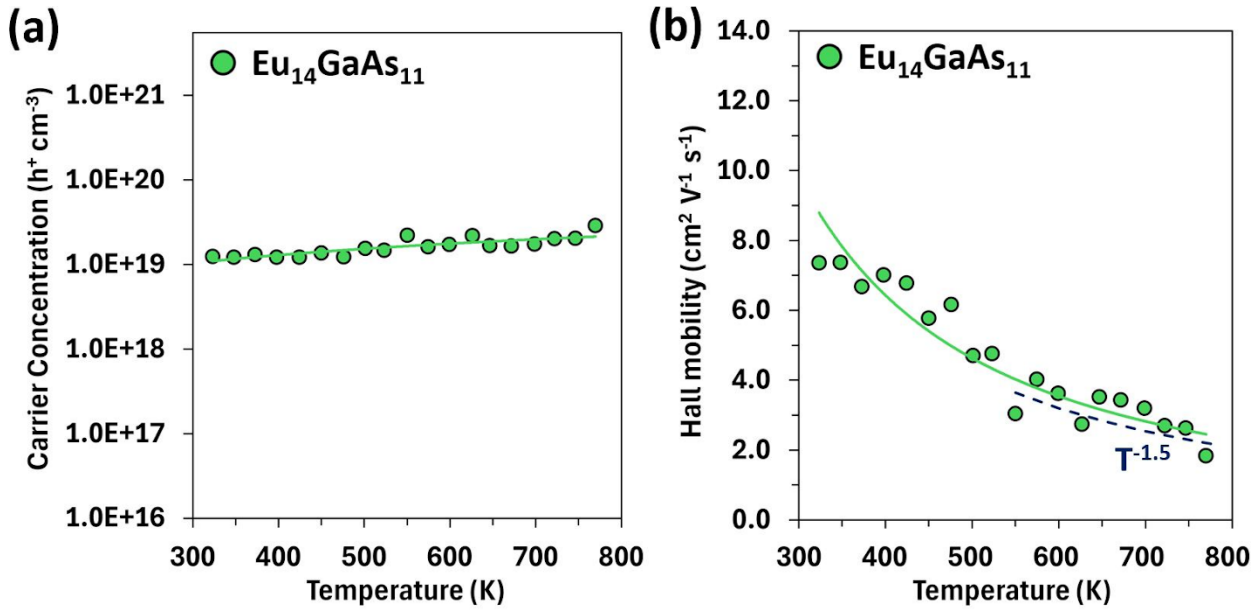


Fig. 5 Temperature-dependent (a) Hall carrier concentration and (b) Hall mobility of $Eu_{14}GaAs_{11}$.

The weighted mobility directly measures the electronic qualities of a thermoelectric material, determined by the experimental values of the Seebeck coefficient and electrical resistivity.[26] For $Eu_{14}GaAs_{11}$, the weighted mobility is measured at 8.38 cm^2 V^{-1} s^{-1} at a temperature of 300 K, as presented in **Fig. 6a**. This weighted mobility decreases at higher temperatures due to increased scattering effects. Additionally, the combination of low weighted mobility and high electrical resistivity results in a relatively low power factor (*PF*) for $Eu_{14}GaAs_{11}$, as depicted in **Fig. 6b**. Initially, the *PF* increases with temperature; however, it begins to decline at high temperatures, as the onset of minority-carriers lowers the *PF* at elevated temperatures.

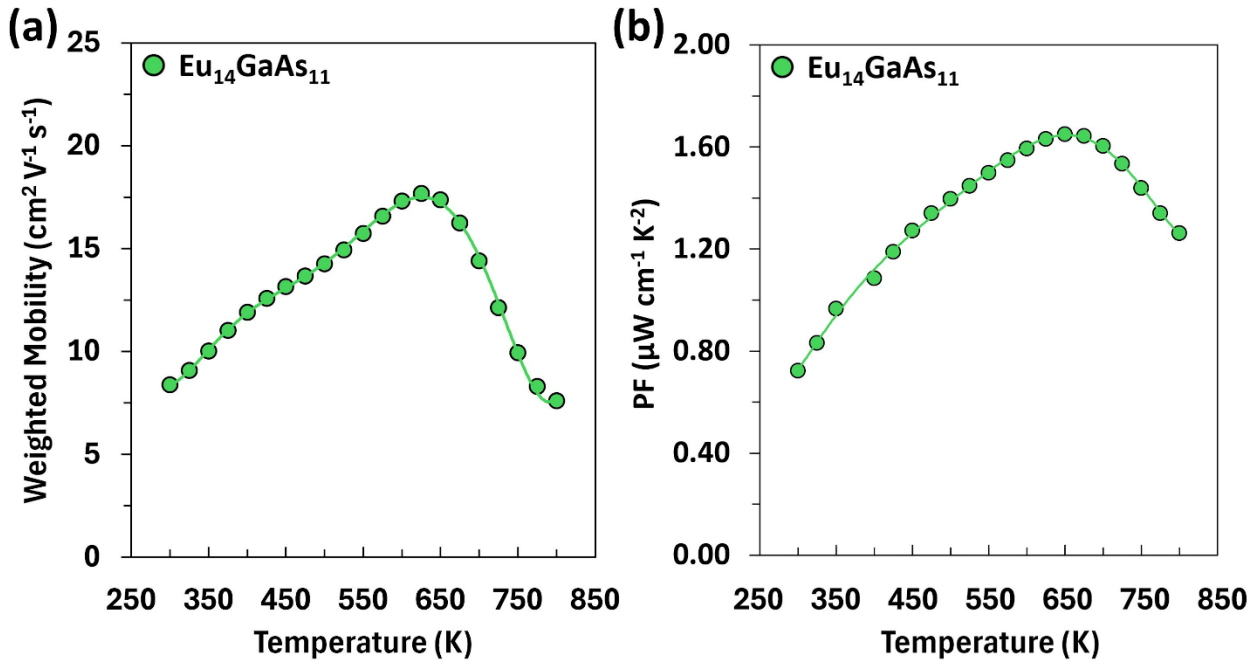


Fig. 6 The (a) weighted mobility and (b) power factor (*PF*) as a function of temperature of $Eu_{14}GaAs_{11}$.

Fig. 7 illustrates the total thermal conductivity (κ_T) of $Eu_{14}GaAs_{11}$. Due to its complex structure, isolated anionic subunits, and a large number of atoms, $Eu_{14}GaAs_{11}$ exhibits an ultra-low thermal conductivity of 0.59 W m^{-1} K^{-1} at room temperature. This value is similar to that of other 14-1-11 compounds.[25] For instance, the thermal conductivity of $Yb_{14}AlSb_{11}$, which contains a trivalent metal ion (M^{3+}) in its subunit, is 0.56 W m^{-1} K^{-1}.[22] Additionally, $Eu_{14}GaAs_{11}$ shows lower thermal conductivity than other ultra-low thermal conductivity Zintl phases, such as $Yb_9Mn_{4.2}Sb_9$ with 0.63 W m^{-1} K^{-1},[27] $Yb_{10}MnSb_9$ with 0.65 W m^{-1} K^{-1},[28] $Ca_{10}CdSb_9$ with 0.70 W m^{-1} K^{-1},[29] and $Ca_{10}AlSb_9$ with 0.75 W m^{-1} K^{-1}.[29] Even when compared to high-performance thermoelectric materials containing divalent metal ions (M^{2+}), such as $Yb_{14}MgSb_{11}$ with a thermal conductivity of 0.70 W m^{-1} K^{-1},[14] $Yb_{14}MnSb_{11}$ with 0.82 W m^{-1} K^{-1},[14] and $Yb_{14}ZnSb_{11}$ with 0.98 W m^{-1} K^{-1},[12] $Eu_{14}GaAs_{11}$ demonstrates a notably lower thermal conductivity. This difference between divalent and trivalent metal ion-containing compounds is expected because fewer electrons are donated to the *p*-type system, as compounds with divalent metal ions typically have a higher hole carrier concentration, leading to a higher electronic contribution to thermal conductivity. The total thermal conductivity decreases with temperature due to acoustic phonon scattering,[30] reaching a minimum of 0.44 W m^{-1} K^{-1} at 923 K. However, at higher temperatures, the total thermal conductivity begins to increase, indicating that bipolar conduction is influencing conductivity within the measured temperature range. The electronic thermal conductivity was estimated using the Wiedemann–Franz relationship, $\kappa_e = L\rho T$, where L is the Lorentz number, ρ is the electrical resistivity, and T is the temperature. The temperature-dependent Lorenz numbers were estimated by assuming acoustic phonon scattering within a single parabolic band model, in which S represents the Seebeck coefficient.[31]

$$L = 1.5 + exp\,[-\frac{|S|}{116}]$$

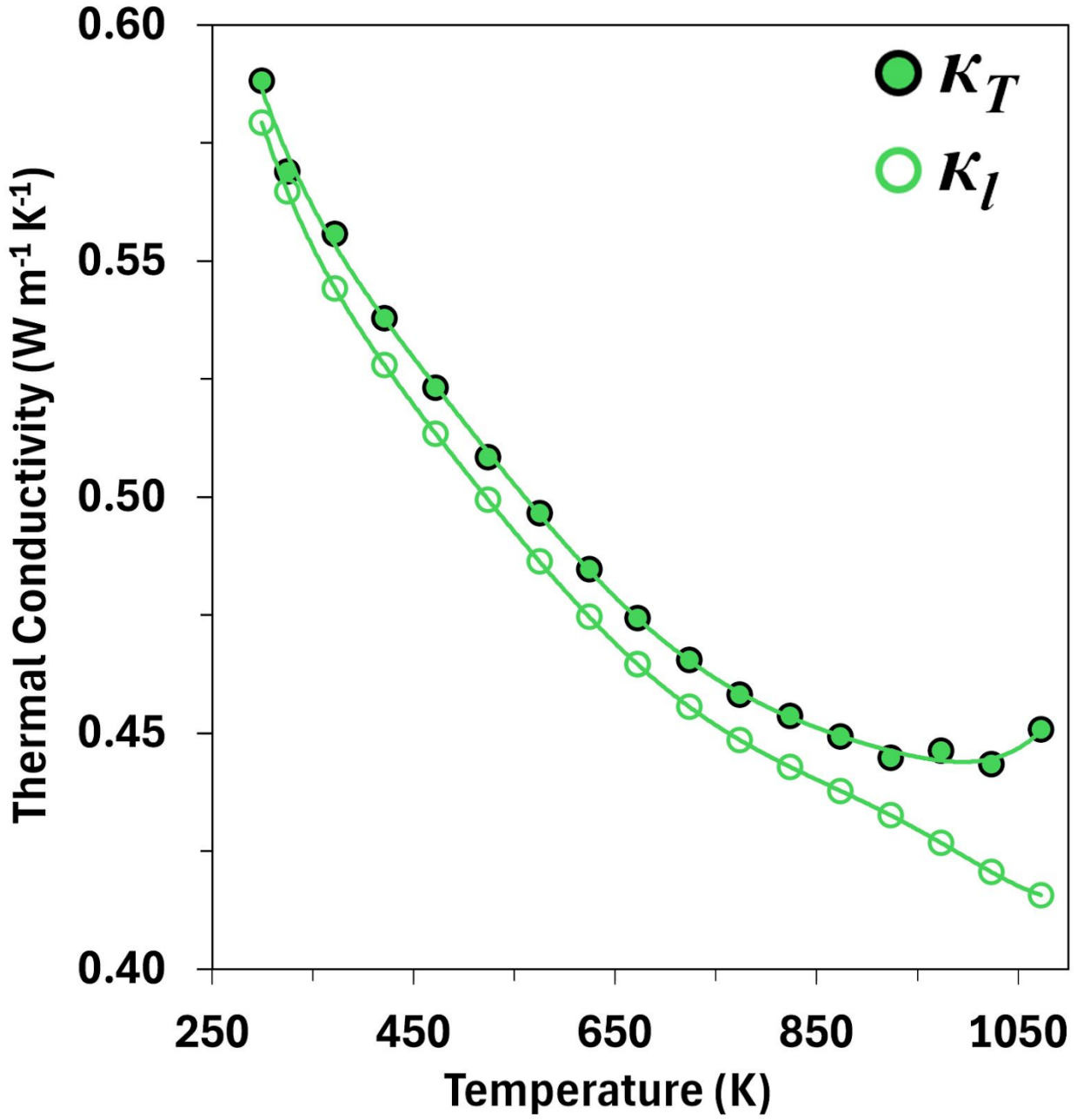


Fig. 7 The total thermal conductivity (κ_T) and the lattice thermal conductivity (κ_l) of $Eu_{14}GaAs_{11}$ as a function of temperature.

The lattice thermal conductivity (κ_l) was obtained by subtracting the electronic thermal conductivity from the total thermal conductivity, as presented in **Fig. 7**. The lattice thermal conductivity of $Eu_{14}GaAs_{11}$ is 0.58 W m^{-1} K^{-1} at room temperature, indicating a minimal electronic contribution to the total thermal conductivity. The low electronic thermal conductivity of the

compound is attributed to its high electrical resistivity. As a result, lattice thermal conductivity becomes the primary contributor to the total thermal conductivity. The intrinsically low lattice thermal conductivity can be attributed to the complex structure of $Eu_{14}GaAs_{11}$, which contains a large number of atoms (N = 208) per unit cell. This results in only three acoustic modes, but an extensive number of optical modes (207 × 3) that are flat and have near-zero velocities, contributing minimally to heat transport.[11]

The thermoelectric figure of merit, zT, for $Eu_{14}GaAs_{11}$ is illustrated and compared to that of some other arsenic-containing Zintl phases in **Fig. 8**. $Eu_{14}GaAs_{11}$ reaches a maximum zT of 0.24 at 725 K before declining due to bipolar conduction. This decline is attributed to the smaller bandgap and the position of the Fermi level, which is near the valence band maximum at the current doping level. In contrast, other 14-1-11 Zintl arsenides, such as $Eu_{14}MgAs_{11}$, $Eu_{14}ZnAs_{11}$, and $Eu_{14}CdAs_{11}$, do not exhibit this decline in zT due to the absence of bipolar conduction.[25] However, $Eu_{14}GaAs_{11}$ demonstrates enhanced thermoelectric performance in the lower temperature range of 300 K to 675 K, especially when compared to $Eu_{14}ZnAs_{11}$.[25] This suggests that, by optimizing the carrier concentration through doping, $Eu_{14}GaAs_{11}$ could potentially maintain its performance by shifting the bend over at much higher temperatures by increasing the bandgap or shifting the Fermi level downwards. Consequently, with appropriate doping, $Eu_{14}GaAs_{11}$ has the potential to achieve higher zT values in the mid-temperature range (725 K).

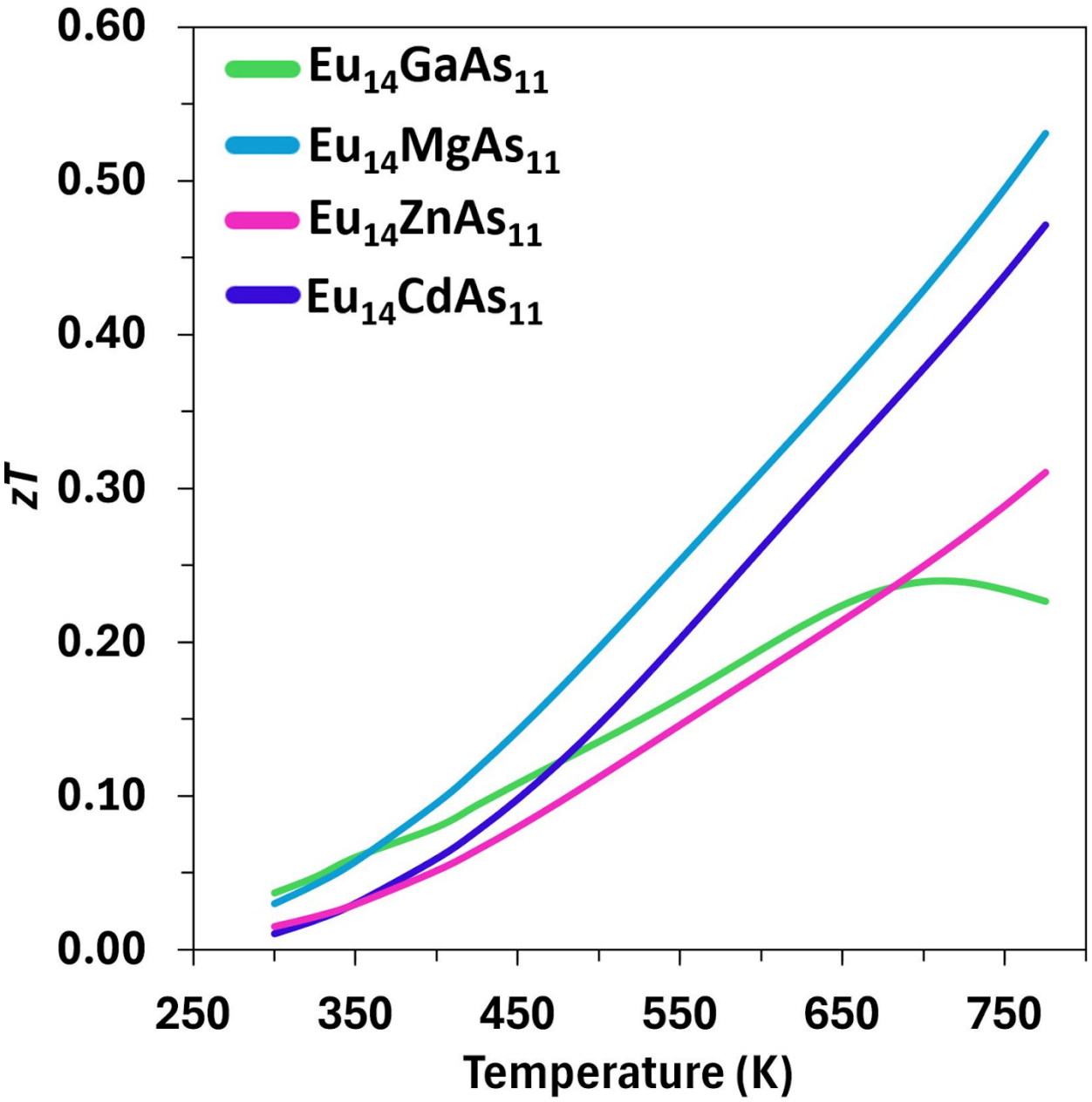


Fig. 8 Temperature-dependent figure of merit *zT* of $Eu_{14}GaAs_{11}$, $Eu_{14}MgAs_{11}$,[25] $Eu_{14}ZnAs_{11}$,[25] and $Eu_{14}CdAs_{11}$.[25]

3 Conclusion

In summary, we introduce a new member of the Zintl 14-1-11 family, the arsenic-containing compound $Eu_{14}GaAs_{11}$, which has been synthesized using a binary precursor-based method involving ball milling and high-temperature annealing. We have investigated its thermal stability and thermoelectric properties to elucidate its electronic and thermal transport properties. Powder X-ray diffraction analysis and Rietveld refinement revealed that this compound, featuring zero-dimensional tetrahedral $[GaAs_4]^{9-}$ subunits, has lattice parameters similar to other Ga-containing

compounds in this family. Notably, this is the first report on the thermoelectric properties of a Ga-containing 14-1-11 phase. $Eu_{14}GaAs_{11}$ exhibits ultra-low thermal conductivity of 0.59 W m^{-1} K^{-1} at room temperature, primarily due to a minimal electronic contribution, with lattice thermal conductivity being the dominant factor. This low thermal conductivity arises from the compound's complex structure, which consists of a large number of atoms, so that only a fractional portion of heat energy is carried by acoustic phonon modes. The resistivity of this compound is high, primarily due to low mobility and carrier concentration. However, it demonstrates a high Seebeck coefficient of 232.80 μV/K at low temperatures, indicating its potential for high thermoelectric efficiency. The thermoelectric efficiency is limited by the onset of bipolar conduction at 713 K, where the Seebeck coefficient reaches a maximum value of 424 μV/K. The onset of minority carriers can be effectively suppressed by adjusting the carrier concentration through appropriate doping. By tuning the carrier concentration, the low power factor of $Eu_{14}GaAs_{11}$ can be enhanced by reducing its resistivity. These findings underscore the promising potential of $Eu_{14}GaAs_{11}$ as a thermoelectric material.

4 Experimental section

4.1 Synthesis and spark plasma sintering

Polycrystalline $Eu_{14}GaAs_{11}$ was synthesized via high-energy ball milling and high-temperature solid-state reactions. All procedures were conducted in an inert atmosphere glove box. High-purity elemental sources, such as Eu ingot (Stanford Advanced Materials, 99.99 %), As chips (Johnson Matthey Chemicals, 99.9999 %), and Ga (Alfa Aesar, 99.99999 %) were used for the synthesis. Binary precursors, EuAs and GaAs, were synthesized by accurately weighing the required stoichiometric amounts of elements with a precision balance and milling them in a 65-cm^3 stainless-steel grinding vial with two stainless steel balls of 12.7 mm using a SPEX 8000D Mixer/Mill for 30 minutes. To ensure homogeneous mixing, the mixture was scraped with a chisel and milled again for an additional hour in the mixer. The resulting homogeneous powder was sealed in a Ta tube and jacketed within an evacuated quartz tube. EuAs was synthesized by annealing at 850 °C for 12 hours, while GaAs was synthesized by annealing at 650 °C for 12 hours. The PXRD patterns of the binary precursors are provided in the SI, **Fig. S1**. $Eu_{14}GaAs_{11}$ was synthesized using the required binary precursors and elements in stoichiometric proportions, following the same procedures described above but annealing at 1100 °C for 96 hours.

The powder compound was densified into pellets by pressing, utilizing a Dr. Sinter Junior Spark Plasma Sintering system (Fuji Electronic Industrial Co., Ltd.) under argon gas. The applied force was increased from 5 kN to 9 kN, and the powder was sintered at 900 °C for 30 minutes. The density of the resulting pellets was determined to be greater than 98% using Archimedes' principle.

Caution: *Arsenic-containing phases can produce toxic arsine gas during reactions. The quartz tube was handled under the fume hood, while the metal tubes were managed inside the glove box. Proper personal protective equipment was worn at all times.*

4.2 Phase characterization

Phase purity and composition were investigated using a Bruker D8 ECO ADVANCE powder X-ray diffraction (PXRD) diffractometer on zero-background off-axis quartz plates, with Cu Kα radiation, over the 2θ angles of 20°−80° with a step size of 0.02°. A portion of the densified pellet was mounted on an epoxy resin disk and polished with 1000-grit sandpaper. It was then further polished using a polishing wheel with 1 μm colloidal diamond suspension. Scanning electron microscopy (SEM) and energy-dispersive X-ray spectroscopy (EDS) were conducted on the polished using a Thermo Fisher Quattro ESEM with a Bruker Quantax EDX detector at an accelerating voltage of 20 kV to analyze phase homogeneity and elemental distribution. The EDS composition analysis is based on the average of data collected from ten points on the pellet.

4.3 Thermogravimetry and differential scanning calorimetry (TG/DSC)

Thermal stability of the sample was analyzed using a Netzsch STA 449 F3 Jupiter. Thermogravimetry and Differential Scanning Calorimetry (TG/DSC) analysis were conducted from room temperature to 900 °C under a flow rate of 50 mL/min of Ar gas. The heating rate was 10K/min.

4.4 Transport properties measurement

Thermal diffusivity was measured using a Netzsch LFA 475 Microflash under Ar flow. To maximize laser absorption, the surface of the pellets was coated with graphite. The total thermal conductivity was calculated using $\kappa = D \times C_p \times r$, where D is the thermal diffusivity, r is the density of the sample, and C_p is the heat capacity of the compound, which was approximated using Dulong-Petit law.

The Seebeck coefficient was measured using a custom-built instrument operating under a controlled low pressure of 300 Torr in a nitrogen atmosphere over a temperature range of 300 K to 775 K.[32] The electrical resistivity and Hall measurements were conducted using an in-house instrument designed based on the van der Pauw geometry.[33] The Hall coefficient measurements were performed with a current of 15-20 mA and a 1 T magnetic field.

Conflicts of interest

The authors declare no competing financial interest.

Data availability

Data for this article, including X-ray powder diffraction, TG/DSC, resistivity, Seebeck coefficient, thermal conductivity, and Hall data, are available at the Dryad repository

Acknowledgements

This work was supported by NSF grants DMR-2307231 and DMR-2350519.

References

1. H. Han, L. Zhao, X. Wu, B. Zuo, S. Bian, T. Li, X. Liu, Y. Jiang, C. Chen, J. Bi, J. Xu and L. Yu, *Journal of Materials Chemistry A*, 2024, **12**, 24041-24083.
2. Q. Yan and M. G. Kanatzidis, *Nature Materials*, 2022, **21**, 503-513.
3. R. Chaliha, M. Kothakonda, C.-W. Lee, J. N. Law, Q. Yang, S. Bobev and P. Gorai, *Journal of Materials Chemistry A*, 2025, **13**, 33385-33396.
4. S. M. Kauzlarich, *Chemistry of Materials*, 2023, **35**, 7355-7362.
5. S. M. Kauzlarich, A. Zevalkink, E. Toberer and G. J. Snyder, in *Thermoelectric Materials and Devices*, eds. I. Nandhakumar, N. M. White and S. Beeby, The Royal Society of Chemistry, 2016, DOI: 10.1039/9781782624042-00001, pp. 1-26.
6. A. P. Justl, G. Cerretti, S. K. Bux and S. M. Kauzlarich, *Journal of Applied Physics*, 2019, **126**.
7. Y. Hu, G. Cerretti, E. L. Kunz Wille, S. K. Bux and S. M. Kauzlarich, *Journal of Solid State Chemistry*, 2019, **271**, 88-102.
8. S. M. Kauzlarich and T. Y. Kuromoto, *Croatica Chemica Acta*, 1991, **64**, 343-352.
9. S. M. Kauzlarich, M. M. Thomas, D. A. Odink and M. M. Olmstead, *Journal of the American Chemical Society*, 1991, **113**, 7205-7208.
10. W. Kim, *Journal of Materials Chemistry C*, 2015, **3**, 10336-10348.
11. M. K. Jana and K. Biswas, *ACS Energy Letters*, 2018, **3**, 1315-1324.
12. A. P. Justl, F. Ricci, A. Pike, G. Cerretti, S. K. Bux, G. Hautier and S. M. Kauzlarich, *Science Advances*, 2022, **8**, eabq3780.
13. M. M. Islam, M. Wróblewska, Z. Shen, E. S. Toberer, V. Taufour and S. M. Kauzlarich, *Chemistry of Materials*, November 22, 2024, DOI: 10.1021/acs.chemmater.4c02200.
14. A. P. Justl, G. Cerretti, S. K. Bux and S. M. Kauzlarich, *Chemistry of Materials*, January 25, 2022, **34**.
15. Y. Hu and S. M. Kauzlarich, *Dalton Transactions*, 2017, **46**, 3996-4003.
16. Y. Hu, J. Wang, A. Kawamura, K. Kovnir and S. M. Kauzlarich, *Chemistry of Materials*, 2015, **27**, 343-351.
17. S. Baranets and S. Bobev, *Materials Today Advances*, 2020, **7**, 100094.
18. S. Baranets, G. M. Darone and S. Bobev, *Journal of Solid State Chemistry*, 2019, **280**, 120990.
19. J. P. A. Makongo, G. M. Darone, S.-Q. Xia and S. Bobev, *Journal of Materials Chemistry C*, 2015, **3**, 10388-10400.
20. B. H. Toby and R. B. Von Dreele, *Journal of Applied Crystallography*, 2013, **46**, 544-549.
21. W. B. Pearson, *Acta Crystallographica*, 1964, **17**, 1-15.
22. C. J. Perez, M. Wood, F. Ricci, G. Yu, T. Vo, S. K. Bux, G. Hautier, G.-M. Rignanese, G. J. Snyder and S. M. Kauzlarich, *Science Advances*, 2021, **7**, eabe9439.
23. E. S. Toberer, S. R. Brown, T. Ikeda, S. M. Kauzlarich and G. Jeffrey Snyder, *Applied Physics Letters*, 2008, **93**.
24. H. J. Goldsmid and J. W. Sharp, *Journal of Electronic Materials*, 1999, **28**, 869-872.
25. M. M. Islam, J. Zheng, A. Pike, K. E. Star, S. K. Bux, G. Hautier and S. M. Kauzlarich, *Journal of the American Chemical Society*, 2025, **147**, 42883-42893.
26. G. J. Snyder, A. H. Snyder, M. Wood, R. Gurunathan, B. H. Snyder and C. Niu, *Advanced Materials*, 2020, **32**, 2001537.
27. S. K. Bux, A. Zevalkink, O. Janka, D. Uhl, S. Kauzlarich, J. G. Snyder and J.-P. Fleurial, *Journal of Materials Chemistry A*, 2014, **2**, 215-220.

28. L. Borgsmiller and G. J. Snyder, *Journal of Materials Chemistry A*, 2022, **10**, 15127-15135.
29. K. Ghosh, L. Borgsmiller, S. Baranets, G. J. Snyder and S. Bobev, *Journal of Materials Chemistry A*, 2024, **12**, 25416-25428.
30. C. Hu, K. Xia, C. Fu, X. Zhao and T. Zhu, *Energy & Environmental Science*, 2022, **15**, 1406-1422.
31. H.-S. Kim, Z. M. Gibbs, Y. Tang, H. Wang and G. J. Snyder, *APL Materials*, 2015, **3**.
32. S. Iwanaga, E. S. Toberer, A. LaLonde and G. J. Snyder, *Review of Scientific Instruments*, 2011, **82**.
33. K. A. Borup, E. S. Toberer, L. D. Zoltan, G. Nakatsukasa, M. Errico, J.-P. Fleurial, B. B. Iversen and G. J. Snyder, *Review of Scientific Instruments*, 2012, **83**.